Contents lists available at [ScienceDirect](https://www.sciencedirect.com)

Journal of Materiomics

journal homepage: www.journals.elsevier.com/journal-of-materiomics/

Highly ordered lead-free double perovskite halides by design

Chang Won Ahn^{a,1}, Jae Hun Jo^{a,1}, Jong Chan Kim^b, Hamid Ullah^c, Sangkyun Ryu^d,
Younghun Hwang^e, Jin San Choi^a, Jongmin Lee^f, Sanghan Lee^f, Hyoungjeen Jeon^d,
Young-Han Shin^c, Hu Young Jeong^b, Ill Won Kim^a, Tae Heon Kim^{a,*}

^a Department of Physics and Energy Harvest-Storage Research Center (EHSRC), University of Ulsan, Ulsan, 44610, Republic of Korea

^b UNIST Central Research Facilities (UCRF) & School of Materials Science and Engineering, Ulsan National Institute of Science and Technology (UNIST), Ulsan, 44919, Republic of Korea

^c Multiscale Materials Modelling Laboratory, Department of Physics, University of Ulsan, Ulsan, 44610, Republic of Korea

^d Department of Physics, Pusan National University, Pusan, 46241, Republic of Korea

^e School of Electrical and Electronics Engineering, Ulsan College, Ulsan, 44610, Republic of Korea

^f School of Materials Science and Engineering, Gwangju Institute of Science and Technology, Gwangju, 61005, Republic of Korea

ARTICLE INFO

Article history:

Received 20 March 2020

Received in revised form

9 May 2020

Accepted 25 May 2020

Available online 24 June 2020

Keywords:

Cs₂AgBiBr₆

Lead-free

Double perovskite

Single crystal

ABSTRACT

Lead-free double perovskite halides are emerging optoelectronic materials that are alternatives to lead-based perovskite halides. Recently, single-crystalline double perovskite halides were synthesized, and their intriguing functional properties were demonstrated. Despite such pioneering works, lead-free double perovskite halides with better crystallinity are still in demand for applications to novel optoelectronic devices. Here, we realized highly crystalline Cs₂AgBiBr₆ single crystals with a well-defined atomic ordering on the microscopic scale. We avoided the formation of Ag vacancies and the subsequent secondary Cs₃Bi₂Br₉ by manipulating the initial chemical environments in hydrothermal synthesis. The suppression of Ag vacancies allows us to reduce the trap density in the as-grown crystals and to enhance the carrier mobility further. Our design strategy is applicable for fabricating other lead-free halide materials with high crystallinity.

© 2020 The Chinese Ceramic Society. Production and hosting by Elsevier B.V. This is an open access article under the CC BY-NC-ND license (<http://creativecommons.org/licenses/by-nc-nd/4.0/>).

1. Introduction

For the last few decades, lead-based perovskite halides CsPbX₃ (X = Cl, Br, I) have been promising candidates in the field of optoelectronic devices, which include photovoltaic solar cells [1–3], X-ray detectors [4–6], and light emitting diodes [7–9]. Despite their excellent functionality (e.g., the high solar-cell efficiency of 23.7%) [10], their use in actual devices has been limited due to the global regulation of toxic lead [11]. Very recently, alternative materials that do not contain a Pb²⁺ ion at the perovskite B-site and are eco-friendly have been under intensive exploration [12–15].

Currently, lead-free double perovskite halides Cs₂AgBiX₆ are of enormous interest as alternatives to lead-based perovskite halides CsPbX₃ [9,16,17]. Here, two neighbouring Pb²⁺ ions in the perovskite halides are alternately replaced with monovalent Ag⁺ and

trivalent Bi³⁺ ions resulting in a double perovskite structure, as shown in Fig. 1a. Some pioneers have already synthesized lead-free double perovskite halide single crystals with good crystallinity. These materials showed fascinating physical properties, including a long lifetime in carrier recombination [18], low effective mass [18], robust phase stability against humidity [18,19], and white-light emission by self-trapped excitons [20]. Nevertheless, Cs₂AgBiX₆ single crystals with better crystallinity are still in demand for potential applications in a wide range of optoelectronic devices [21]. To achieve this, a systematic study of the synthesis of highly crystalline Cs₂AgBiX₆ single crystals is essential.

The structural stability of lead-free double perovskite halide Cs₂AgBiX₆ is very susceptible to changes in the ambient chemical composition during single crystal growth. It has been theoretically demonstrated that various defects in a double perovskite Cs₂AgBiBr₆ can be created, such as Ag vacancies, Bi vacancies, and Ag_{Bi} anti-site defects [22]. Note that their formation energies in theoretical calculations are dependent on a particular chemical condition (e.g., Ag-rich and Bi-rich). It is also interesting that the formation energies of secondary phases, which include CsAgBr₂

* Corresponding author.

E-mail address: thkim79@ulsan.ac.kr (T.H. Kim).

Peer review under responsibility of The Chinese Ceramic Society.

¹ These authors contributed equally to this work.

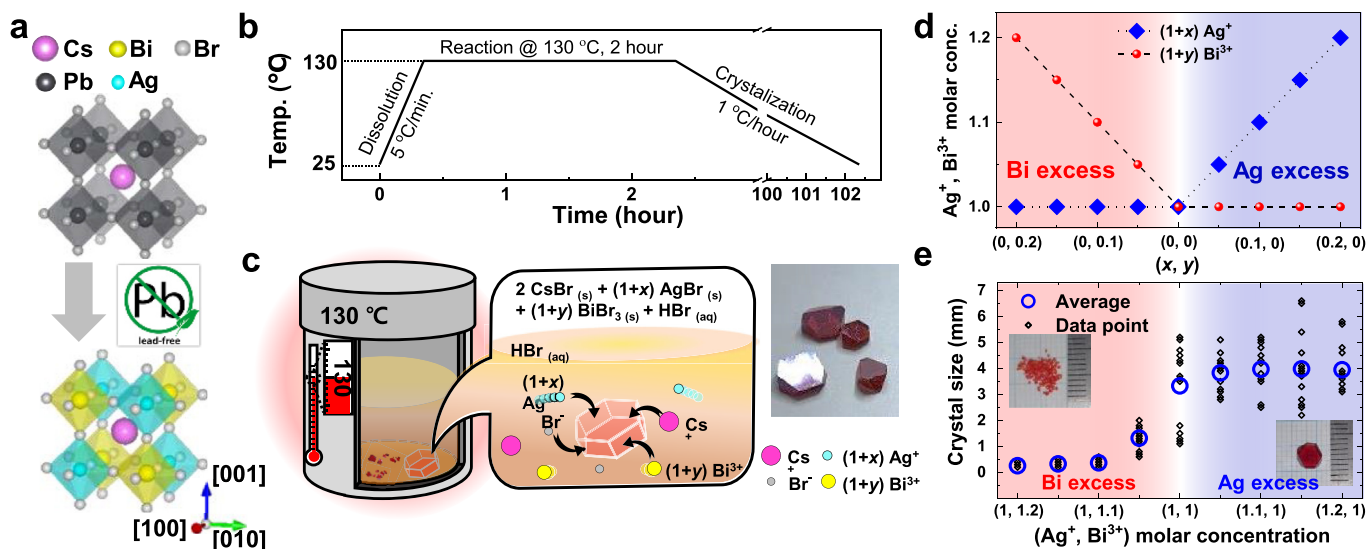


Fig. 1. Lead-free double perovskite halide crystal growth. (a) Schematic view of lead-based perovskite halide CsPbBr_3 and lead-free double perovskite halide $\text{Cs}_2\text{AgBiBr}_6$. (b) Temperature-time sequence diagram for the hydrothermal synthesis of $\text{Cs}_2\text{AgBiBr}_6$. (c) A schematic diagram of a crystallization process for $\text{Cs}_2\text{AgBiBr}_6$ double perovskite formation and optical image of the crystals. (d) Initial molar concentrations of Ag^+ and Bi^{3+} ions in the precursor solution to generate excess Ag or Bi conditions in a hydrothermal reaction. (e) The lateral sizes of $\text{Cs}_2\text{AgBiBr}_6$ crystals according to the initial molar concentrations of Ag^+ and Bi^{3+} ions in a hydrothermal reaction.

(tetragonal, $P4/nmm$) [23], Cs_2AgBr_3 (orthorhombic, $Pnma$) [23], and $\text{Cs}_3\text{Bi}_2\text{Br}_9$ (trigonal, $P-3m1$) [24], compete with that of $\text{Cs}_2\text{AgBiBr}_6$ in the thermodynamic reaction process. Furthermore, it appears that the most energetically stable phase is very different relying on the given chemical environment. Despite these intriguing thermodynamic calculations of the phase stability in lead-free double perovskite halides, it has rarely been examined how the structural phase of $\text{Cs}_2\text{AgBiX}_6$ during crystal growth evolves depending on variations in either the Ag^+ or Bi^{3+} content.

It is worth noting that the chemical stoichiometry and crystallinity of $\text{Cs}_2\text{AgBiX}_6$ single crystals can strongly depend on the compositional ratio between Ag^+ and Bi^{3+} ions during crystal growth. Due to the high ionic conductivity of Ag^+ ions [25–27], some of the mobile Ag^+ ions would not participate in the crystallization, and then the rate of chemical reaction can be dependent on the total amount of Ag^+ cations inside a precursor solution. Although a stoichiometric amount of Ag^+ ions is incorporated in the precursor solution, the resulting $\text{Cs}_2\text{AgBiX}_6$ crystal will be Ag-deficient (i.e., Bi-excessive) due to the itinerant Ag^+ ions. This results in poor crystallinity with the appearance of impurity/secondary phases. On the other hand, it is well known that a transition-metal Bi atom is very volatile, and thus it can be easily vaporized in a thermally-assisted chemical reaction process [28–30]. To avoid Bi deficiency in the end product, a high content of Bi^{3+} ions exceeding the stoichiometric composition was added in the beginning stage of material synthesis [28–30]. Therefore, it is of great interest to investigate the effect of the initial Ag^+ or Bi^{3+} content on the chemical composition and structural phases of the as-grown $\text{Cs}_2\text{AgBiX}_6$ single crystals.

In this work, we experimentally demonstrated the impact of Ag-excess or Bi-excess on the single crystal growth of a lead-free double perovskite halide $\text{Cs}_2\text{AgBiBr}_6$. While tuning the molar concentration of the reactants (i.e., CsBr , AgBr and BiBr_3) in the hydrothermal synthesis of $\text{Cs}_2\text{AgBiBr}_6$, we systematically monitored how its crystal growth evolved as a function of the initial contents of the Ag and Bi elements in the AgBr and BiBr_3 , respectively. Note that an Ag-rich (Bi-rich) environment is attainable in the as-prepared precursor solution for the hydrothermal reaction, as the concentration of the starting material AgBr (BiBr_3) exceeds the

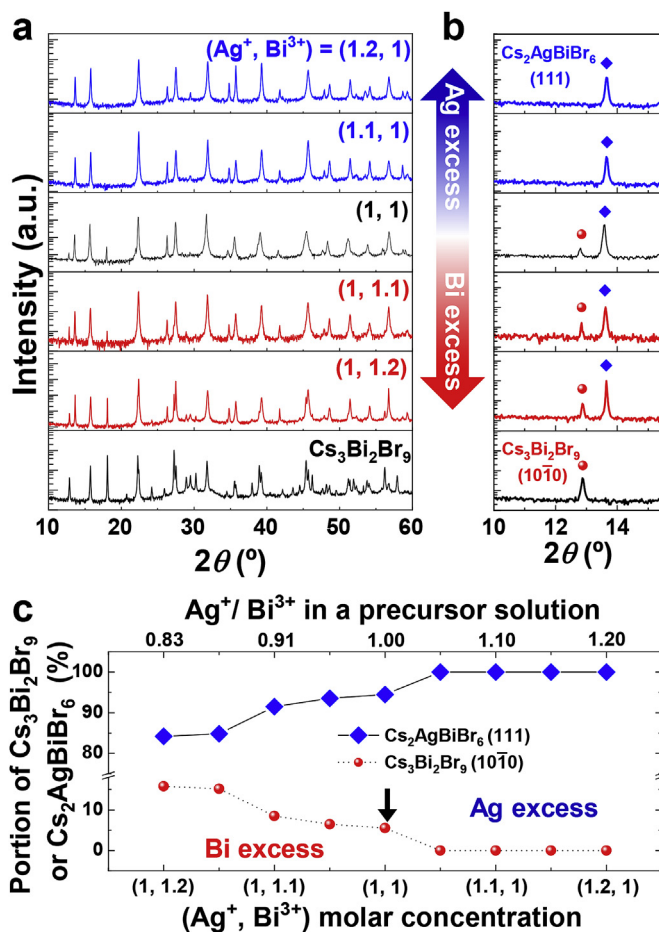


Fig. 2. Structure characterization. (a) X-ray diffraction patterns of ground powder of $\text{Cs}_2\text{AgBiBr}_6$ single crystals grown under various chemical environments (i.e., stoichiometric, excess Bi, and excess Ag conditions), and $\text{Cs}_3\text{Bi}_2\text{Br}_9$ powder (as a reference for the secondary phase). (b) Enlarged view of the XRD peak corresponding to the (111) Bragg peak of $\text{Cs}_2\text{AgBiBr}_6$ and (10T0) Bragg peak of $\text{Cs}_3\text{Bi}_2\text{Br}_9$ around a 2θ angle of 13° . (c) The volume fractions between the primary $\text{Cs}_2\text{AgBiBr}_6$ and secondary $\text{Cs}_3\text{Bi}_2\text{Br}_9$ phases based on the initial molar concentrations of Ag^+ and Bi^{3+} ions in a hydrothermal reaction.

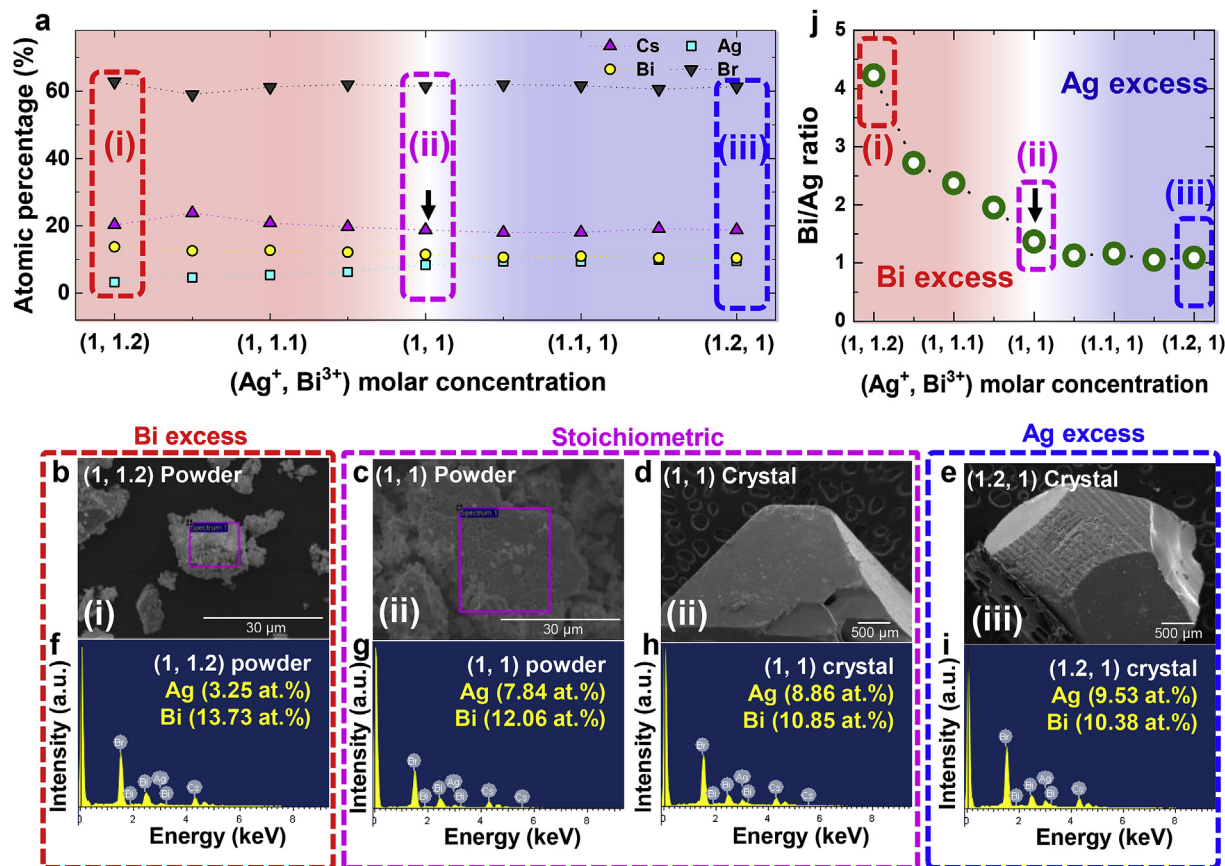


Fig. 3. Composition analysis. (a) Atomic composition as a function of the initial molar concentrations of Ag⁺ and Bi³⁺ ions in the as-grown Cs₂AgBiBr₆ powders and single crystals via a hydrothermal reaction. (b, c, d, e) SEM images and (f, g, h, i) EDX spectra of Cs₂AgBiBr₆ powders and crystals grown under various chemical environments [i.e., Bi-excess (b, f), stoichiometric (c, d, g, h), and Ag-excess (e, i) conditions]. (j) The estimated molar ratio of Bi/Ag as a function of the initial molar concentrations of Ag⁺ and Bi³⁺ ions in as-grown Cs₂AgBiBr₆ samples.

stoichiometric amount. We found that the degree of crystallization strongly depended on the initial reaction conditions. It appears that the as-grown Cs₂AgBiBr₆ single crystals under Ag-rich conditions are highly crystalline with a well-defined double perovskite structure microscopically. In contrast, under Bi-rich conditions, the crystallization of Cs₂AgBiBr₆ is relatively poor with the formation of a parasitic Cs₃Bi₂Br₉ phase. We also identified that the Cs₂AgBiBr₆ single crystals synthesized under Ag-excess conditions exhibited a larger indirect band gap ($E_{g,indirect} \sim 2.12$ eV) than those ($E_{g,indirect} \sim 2.07$ eV) synthesized under the stoichiometric conditions, which is close to the value predicted ($E_{g,indirect} \sim 2.26$ eV) by theoretical calculations. A possible origin of such a difference in the crystallinity of Cs₂AgBiBr₆ will be discussed in conjunction with its effect on the electrical transport properties (e.g., carrier mobility) of the as-grown single crystals.

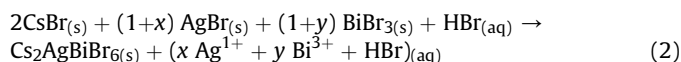
To fabricate lead-free double perovskite halide Cs₂AgBiBr₆ single crystals, we used a conventional hydrothermal reaction technique. In the hydrothermal method, a reactant solution in a Teflon vessel was pressurized with an autoclave during the crystal growth. Under the internal pressure imposed by the autoclave, a double perovskite Cs₂AgBiBr₆ phase was easily stabilized, enabling the subsequent growth of single crystals. For the hydrothermal reaction, we first prepared a starting solution by dissolving high-purity CsBr (99.9%), AgBr (99.0%), and BiBr₃ ($\geq 98.0\%$) powders in a buffered HBr solvent (the HBr weight percentage of 48% in H₂O) [18]. As shown in Fig. 1b, the as-prepared precursor solution was fired in a box furnace up to 130 °C with a ramping rate of 5 °C/min. Then, it was cooled down to room temperature with a ramping rate of 1 °C/hour for

crystallization. For more details related to the single crystal growth, see the method section and Fig. S1 (Supporting Information).

In the hydrothermal synthesis of Cs₂AgBiBr₆ single crystals, it is possible to control the initial chemical environment of the reaction. A chemical reaction between the starting substances (i.e., CsBr, AgBr, and BiBr₃) produces a stoichiometric Cs₂AgBiBr₆ as follows [22]:



Note that the ratio of molar concentrations between AgBr and BiBr₃ is 1 in the stoichiometric case. We stress that it is important to assess the degree of crystallization of double perovskite halides depending on the initial concentrations of Ag⁺ and Bi³⁺ ions that take part in a chemical reaction. Thus, we produced an excess Ag or excess Bi condition while varying the molar concentrations of the AgBr and BiBr₃ reactants in a precursor solution as follows (Fig. 1c):



Herein, the x (y) value was varied from 0.05 to 0.20 with increments of 0.05 in the Ag (Bi)-excess condition, whereas the y (x) value was fixed to zero, as shown Fig. 1d. For example, when the x and y values were 0.05 and 0.00, respectively, the corresponding molar concentrations of $(1+x)$ AgBr and $(1+y)$ BiBr₃ reactants became 1.05 and 1.00, respectively, which allowed us to artificially generate the Ag-excess condition in the hydrothermal reaction. In the opposite

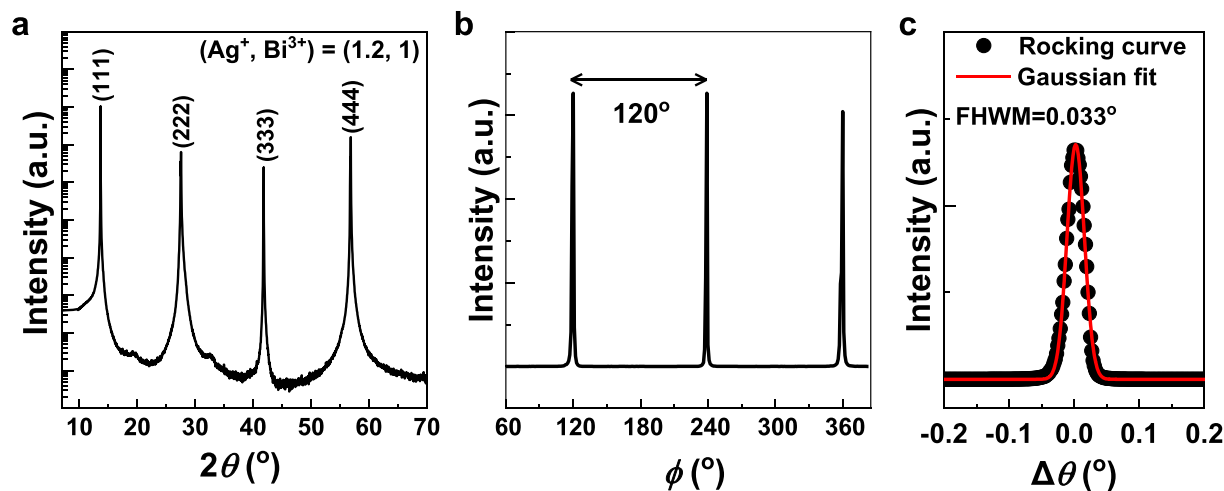


Fig. 4. Crystallinity of our $\text{Cs}_2\text{AgBiBr}_6$ single crystal grown under an Ag-excessive environment. The high-resolution XRD data of (a) the θ - 2θ scan, (b) the phi (ϕ) scan, and (c) the rocking-curve measurement of the $\text{Cs}_2\text{AgBiBr}_6$ single crystal grown under an Ag-excessive environment.

case (i.e., $x = 0$ and $y > 0$), the Bi-excess condition was attainable as well.

We found that the lateral sizes of $\text{Cs}_2\text{AgBiBr}_6$ single crystals grown by a hydrothermal method strongly depended on the initial molar concentrations of AgBr and BiBr_3 reactants (Fig. 1e). More details of the size estimation of the as-grown $\text{Cs}_2\text{AgBiBr}_6$ single crystals are described in Fig. S2 (Supporting Information). It is also interesting that the double perovskite $\text{Cs}_2\text{AgBiBr}_6$ phase is highly crystallized with an average lateral dimension of ~ 4 mm under an excess Ag environment only, although there were some variations in the measured crystal size (the measured values of the lateral sizes of all $\text{Cs}_2\text{AgBiBr}_6$ crystals used in this work are shown in Table S1). In contrast, under excess Bi conditions, the crystallinity of the as-produced $\text{Cs}_2\text{AgBiBr}_6$ crystals was very poor and still remained in a powder form. For the stoichiometric case, where the molar ratio between Ag^+ and Bi^{3+} contents was 1, the measured crystal size quite varied significantly from ~ 1 to ~ 5 mm, indicating that it was difficult to achieve reproducible growth of $\text{Cs}_2\text{AgBiBr}_6$ single crystals with high crystallinity.

2. Results and discussion

Fig. 2a shows the powder x-ray diffraction (XRD) results of $\text{Cs}_2\text{AgBiBr}_6$ single crystals grown under various chemical environments (i.e., stoichiometric, excess Bi, and excess Ag conditions). To perform these measurements, $\text{Cs}_2\text{AgBiBr}_6$ single crystals were first synthesized using a precursor solution with different molar concentrations of Ag^+ [(1+x)] and Bi^{3+} [(1+y)] ions by a hydrothermal method; then, we prepared $\text{Cs}_2\text{AgBiBr}_6$ powders by grinding the as-grown $\text{Cs}_2\text{AgBiBr}_6$ single crystals (for more details of the synthesis of $\text{Cs}_2\text{AgBiBr}_6$ single crystals, see the method section in Supporting Information). We found that the obtained powder XRD patterns (the blue solid lines) of $\text{Cs}_2\text{AgBiBr}_6$ single crystals grown under Ag-excess conditions exactly matched that of a cubic $\text{Cs}_2\text{AgBiBr}_6$ phase ($a = b = c = 11.25$ Å) (detailed analyses of powder XRD results, Fig. S3, Supporting Information) [18]. In contrast, it appeared that the as-grown $\text{Cs}_2\text{AgBiBr}_6$ single crystals under Bi-excess conditions contained a secondary $\text{Cs}_3\text{Bi}_2\text{Br}_9$ phase (marked by the red solid circles) and a little amount of BiBr_3 residues (Fig. S3b, Supporting Information) in addition to the major double perovskite phase (marked by the blue solid diamonds) (Fig. 2b). For comparison, the measured XRD pattern of $\text{Cs}_3\text{Bi}_2\text{Br}_9$ powders is shown in the lowest panel of Fig. 2a (a detailed comparison of the obtained XRD

patterns of $\text{Cs}_2\text{AgBiBr}_6$ powders with the reference XRD pattern of $\text{Cs}_3\text{Bi}_2\text{Br}_9$ is provided in Fig. S4, Supporting Information).

Fig. 2c shows the volume fractions of the primary $\text{Cs}_2\text{AgBiBr}_6$ and secondary $\text{Cs}_3\text{Bi}_2\text{Br}_9$ phases. We estimated the relative portions of $\text{Cs}_2\text{AgBiBr}_6$ and $\text{Cs}_3\text{Bi}_2\text{Br}_9$ phases by fitting the (111) and (10 $\bar{1}$ 0) Bragg peaks (around the 2θ angle of 13°) of double perovskite $\text{Cs}_2\text{AgBiBr}_6$ and layered perovskite $\text{Cs}_3\text{Bi}_2\text{Br}_9$ phases using a Lorentzian distribution function. It is evident that the volume fraction of the primary $\text{Cs}_2\text{AgBiBr}_6$ (the secondary $\text{Cs}_3\text{Bi}_2\text{Br}_9$) phase keeps increasing (decreasing) as the molar concentration of Bi^{3+} ions decreases from 1.2 to 1.0 under excess Bi conditions. Here, the molar content of Ag^+ ions relative to the Bi content increased, although the absolute molar concentration of Ag^+ ions was fixed at 1. It is also noticeable that the secondary $\text{Cs}_3\text{Bi}_2\text{Br}_9$ phase (the extracted volume fraction of $\sim 4\%$) still remains in $\text{Cs}_2\text{AgBiBr}_6$ single crystals synthesized under stoichiometric conditions (denoted by a black arrow). In contrast, there is no $\text{Cs}_3\text{Bi}_2\text{Br}_9$ phase in the as-grown single crystals under excess Ag conditions, and the $\text{Cs}_2\text{AgBiBr}_6$ phase becomes dominant. This indicates that the phase stability of double perovskite $\text{Cs}_2\text{AgBiBr}_6$ is very susceptible to the initial chemical concentrations in the precursor solution prepared for the hydrothermal reaction.

To gain further insight into the chemical-environment-dependent structural instability in $\text{Cs}_2\text{AgBiBr}_6$ single crystals, we carried out energy-dispersive x-ray spectroscopy (EDX) measurements to analyze the chemical stoichiometry. As shown in Fig. 3a, the element-specific EDX results reveal that the Ag and Bi contents in the as-synthesized $\text{Cs}_2\text{AgBiBr}_6$ compounds are very different depending on the initial molar concentrations of Ag^+ and Bi^{3+} ions in a precursor solution. On the other hand, there was no significant change in the measured Cs and Br contents, which are almost constant with atomic percentages of 20% and 60%, respectively [For the stoichiometric analyses of as-synthesized $\text{Cs}_2\text{AgBiBr}_6$ single-crystal/powder compounds, we carried out scanning electron microscopy (SEM) and EDX measurements. And, the obtained SEM images and EDX spectra are shown in Fig. 3b–i]. Considering the fact that the atomic percentages of Cs, Ag, Bi, and Br elements are 20%, 10%, 10%, and 60% in stoichiometric $\text{Cs}_2\text{AgBiBr}_6$, respectively, all the $\text{Cs}_2\text{AgBiBr}_6$ single-crystal/powder specimens should contain stoichiometric amount of Cs^+ and Br^- ions.

To further assess either Bi or Ag deficiencies in the $\text{Cs}_2\text{AgBiBr}_6$ compounds, we also calculated the proportion of Bi to Ag contents from the measured atomic percentages of Bi and Ag elements

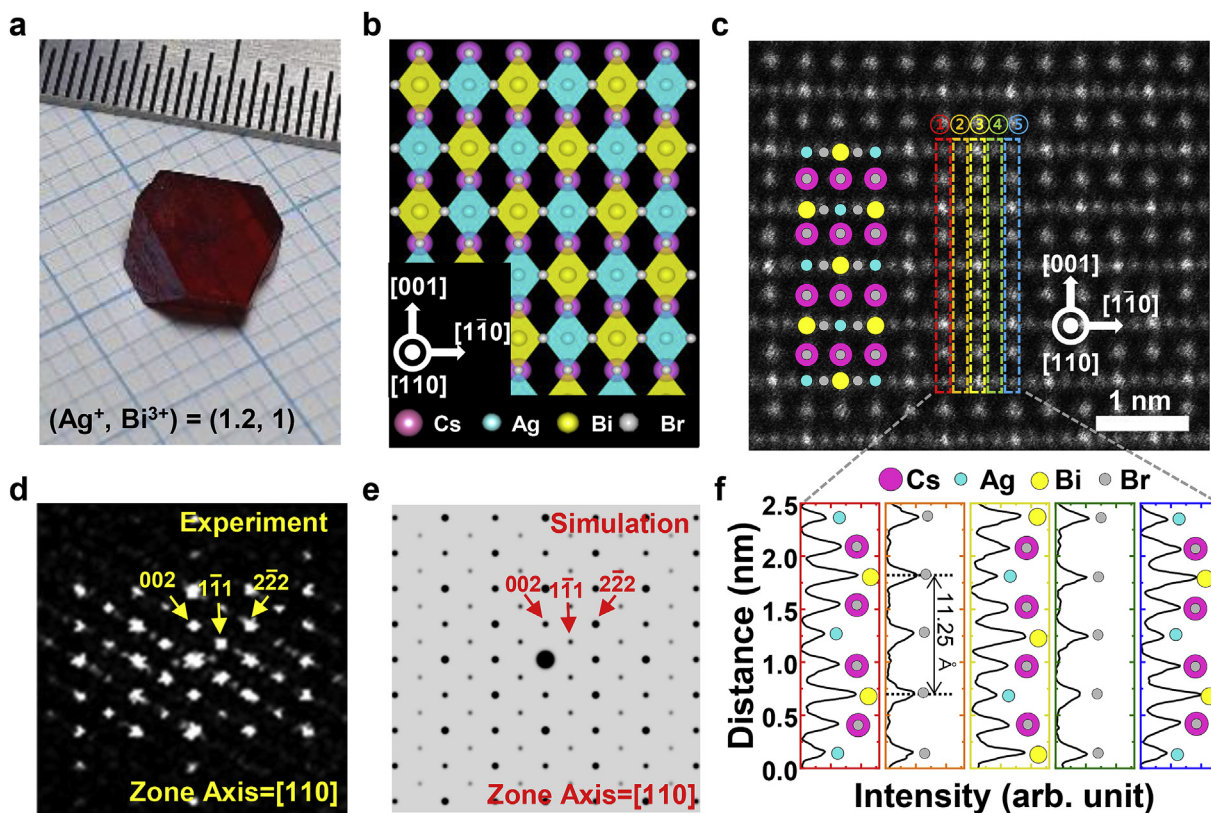


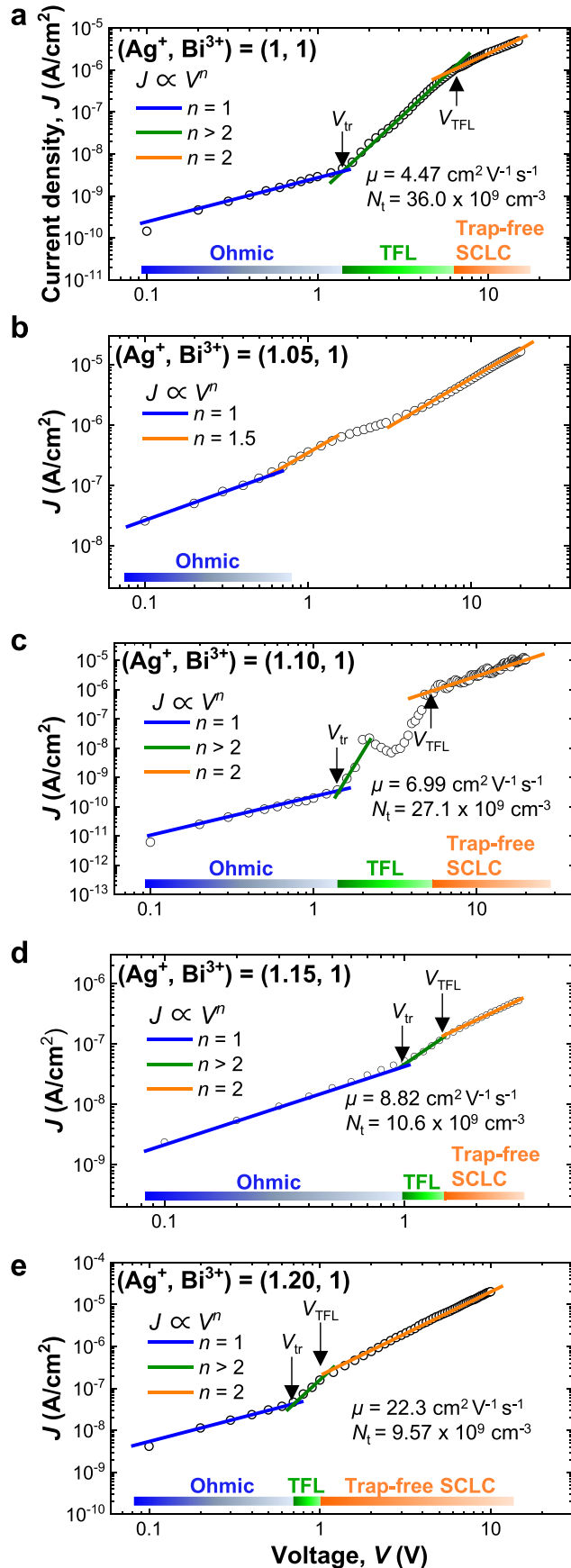
Fig. 5. Atomic-resolution STEM images of a $\text{Cs}_2\text{AgBiBr}_6$ single crystal grown under an Ag-excess environment. (a) Optical image of $\text{Cs}_2\text{AgBiBr}_6$ single crystals. (b) Schematic diagram of the $\text{Cs}_2\text{AgBiBr}_6$ structure viewed along the $[110]$ direction. (c) High-resolution HAADF-STEM image. (d) FFT pattern of the $\text{Cs}_2\text{AgBiBr}_6$ single crystals, and (e) simulated electron diffraction pattern of a cubic double perovskite structure along the $[110]$ zone axis. (f) HAADF-STEM intensity profiles along the $[001]$ direction from regions shown in (c) corresponding to the atomic rows shown in the schematic.

(Fig. 3j). For $\text{Cs}_2\text{AgBiBr}_6$ single crystals grown under excess Ag conditions, the atomic percentages of Ag and Bi elements are the same (approximately 10%), and the derived Bi/Ag values are close to 1, indicating that there are no Bi and Ag vacancies inside the as-grown single crystals. In contrast, it is clear that the Bi and Ag ratio is larger than 1 for $\text{Cs}_2\text{AgBiBr}_6$ compounds synthesized under both excess Bi and stoichiometric (denoted by a black arrow) conditions. This indicates that the measured single crystal/powder specimens have excessive Bi (*i.e.*, Ag-deficient) elements due to the presence of the secondary $\text{Cs}_3\text{Bi}_2\text{Br}_9$ phase.

High-resolution XRD measurements were performed to macroscopically examine the crystallinity of our $\text{Cs}_2\text{AgBiBr}_6$ single crystals (for details related to the XRD experiments, see the method section in Supporting Information). For these XRD analyses, we first selected a $\text{Cs}_2\text{AgBiBr}_6$ single crystal synthesized under an excess Ag condition where the initial molar concentrations of Ag^+ and Bi^{3+} ions were 1.2 and 1.0, respectively. Note that $\text{Cs}_2\text{AgBiBr}_6$ single crystals grown under excess Ag conditions were well crystallized with no impurity phases, whereas the as-grown single crystals under excess Bi and stoichiometric conditions were poorly crystallized and showed a secondary $\text{Cs}_3\text{Bi}_2\text{Br}_9$ phase (Fig. 2a). The subsequent XRD θ - 2θ result clearly shows that the as-grown $\text{Cs}_2\text{AgBiBr}_6$ single crystals in an excess Ag environment are single-crystalline with a $[111]$ crystallographic orientation (Fig. 4a). An XRD ϕ (ϕ) scan of the (220) Bragg peak shows 3-fold symmetry due to the preferred $[111]$ orientation in a cubic double perovskite structure (Fig. 4b). The as-grown single crystal should be in a single domain state structurally, because no diffraction peak due to in-plane misorientation was observed except for the three $\{220\}$ Bragg peaks. To evaluate the mosaicity of our $\text{Cs}_2\text{AgBiBr}_6$

single crystals, we also carried out XRD rocking-curve measurements of the (111) Bragg peak, as shown in Fig. 4c. The measured diffraction peak is very sharp, and then the estimated full width at half maximum (FWHM) via the best fit was 0.03° , which is smaller than the FWHM values of previously reported $\text{Cs}_2\text{AgBiBr}_6$ (0.06°) single crystal [31], lead-based perovskite halide CsPbBr_3 (0.16°) [32], $\text{CH}_3\text{NH}_3\text{PbBr}_3$ (0.07°). This peak is comparable to conventional perovskite oxide LiNbO_3 (0.02°) [33] and SrTiO_3 (0.01°) single crystals (XRD rocking-curve results of $\text{CH}_3\text{NH}_3\text{PbBr}_3$ and SrTiO_3 single crystals are shown in Fig. S5, Supporting Information). Accordingly, it is highly likely that there is no mosaic spread in our $\text{Cs}_2\text{AgBiBr}_6$ single crystals, and they should be highly crystallized with a single domain configuration.

To visualize the atomic structure in our $\text{Cs}_2\text{AgBiBr}_6$ single crystals, we carried out cross-sectional scanning transmission electron microscopy (STEM) experiments (sample preparation and STEM measurement details are provided in the method section and Fig. S6, Supporting Information). As with the XRD analyses, we used a high crystalline $\text{Cs}_2\text{AgBiBr}_6$ single crystal synthesized under excess Ag conditions for the STEM measurements (Fig. 5a). In double perovskite $\text{Cs}_2\text{AgBiBr}_6$, two neighbouring halogen octahedra [*i.e.*, AgBr_6 (light cyan diamonds) and BiBr_6 (light yellow diamonds)] are alternately interconnected *via* corner sharing, resulting in an octahedral breathing order, as shown in Fig. 5b. A high-angle annular dark field (HAADF)-STEM image of the as-grown $\text{Cs}_2\text{AgBiBr}_6$ single crystal reveals that the observed atomic configuration (Fig. 5c) is in good agreement with the projected lattice structure (Fig. 5b) along the $[110]$ zone axis. It is worth noting that all the chemical elements (Cs, Ag, Bi, and Br) constituting $\text{Cs}_2\text{AgBiBr}_6$ single crystals are uniformly distributed



throughout the whole region of the specimen with no spatial inhomogeneity (details about the STEM-EDX measurements are provided in Fig. S7, Supporting Information). In a fast Fourier transform (FFT) pattern obtained from the HAADF-STEM image, we observed $\{111\}$ diffraction peaks arising from the lattice doubling of simple perovskite unit cells (Fig. 5d). We also found that the FFT pattern corresponded to the simulated electron diffraction pattern of a cubic double perovskite structure (Fig. 5e) (a comparison between the simulated electron diffraction patterns of cubic perovskite and double perovskite structures is shown in Fig. S8, Supporting Information).

To identify the atomic arrangement of the as-grown $\text{Cs}_2\text{AgBiBr}_6$ single crystals, we plot the line profiles of the measured STEM intensity in a HAADF image (Fig. 5c) along the cubic $[001]$ direction, as shown in Fig. 5f. Note that a $\text{Cs}_2\text{AgBiBr}_6$ unit cell can be conceptually viewed as a stack of CsBr-BiBr_2 (or AgBr_2)- CsBr-AgBr_2 (or BiBr_2) in the $[001]$ direction. Considering the fact that the peak intensities of atoms in the extracted line profiles are determined by the atomic number (Z) [34], the atomic stacking sequences in columns 1 (the red dashed box in Fig. 5c) and 5 (the blue dashed box in Fig. 5c) should correspond to Cs-Bi-Cs-Ag. And, in column 3 (the yellow dashed box in Fig. 5c), the corresponding stacking sequence becomes Cs-Ag-Cs-Bi. When the $\text{Cs}_2\text{AgBiBr}_6$ unit cell is projected along the $[110]$ zone axis, halogen Br atoms only appear with an interatomic spacing of $11.25 \text{ \AA}/2$ (i.e., a half lattice parameter of cubic $\text{Cs}_2\text{AgBiBr}_6$) [18], as displayed in columns 2 (the orange dashed box in Figs. 5c) and 4 (the green dashed box in Fig. 5c). Furthermore, in the intensity profiles, the peak position of each atom is very periodic, and there was no variation in the peak intensity. It follows that all the constituent atoms in our $\text{Cs}_2\text{AgBiBr}_6$ single crystals are highly ordered at the atomic level, resulting in the well-defined double perovskite structure.

Fig. 6 shows space-charge-limited bulk conduction (SCLC) behaviors of $\text{Cs}_2\text{AgBiBr}_6$ single crystals synthesized under stoichiometric $[(\text{Ag}^+, \text{Bi}^{3+}) = (1, 1)]$ (Fig. 6a) and Ag-excess $[(\text{Ag}^+, \text{Bi}^{3+}) = (1.05, 1), (1.1, 1), (1.15, 1), \text{ and } (1.2, 1)]$ (Fig. 6b-e) conditions, respectively. Note that the majority of the conduction carriers are holes (i.e., p-type) in $\text{Cs}_2\text{AgBiBr}_6$, because the valence band maximum is close to the Fermi level (the calculated electronic band structure of $\text{Cs}_2\text{AgBiBr}_6$ is shown in Fig. S9, Supporting Information) [31,35]. A metal-insulator-metal (MIM) structure of $\text{Au}/\text{Cs}_2\text{AgBiBr}_6/\text{Au}$ is commonly used for the hole-governing electrical transport measurements (for more details on our current density-voltage (J - V) measurements, see the method section and Fig. S10, Supporting Information) [31,36]. In the conventional SCLC model [37–40], the J - V curves at low voltages (i.e., $V < V_{\text{tr}}$) are characterized by linear ohmic behaviors ($J_{\text{ohm}} \propto V$). As the voltage increases across a transition voltage of V_{tr} , the deep traps begin to fill, resulting in trap-filled-limited currents ($J_{\text{TFL}} \propto V^n$ with $n > 2$). At even higher voltages (i.e., $V > V_{\text{TFL}}$), the deep traps are almost totally filled, exhibiting deep-trap-free-conduction behavior (i.e., space-charge-limited currents, $J_{\text{SCL}} \propto V^2$). In this space-charge-limited region, the dark current density (J_D fitted by the Mott-Gurney law and V_{TFL}) [37–40] is described as follows:

$$J_D = \frac{9\epsilon\epsilon_0\mu V^2}{8L^3} \quad (3)$$

Fig. 6. Carrier mobility characterization. Logarithm J - V curves in the dark for $\text{Cs}_2\text{AgBiBr}_6$ single crystals grown under (a) stoichiometric and (b, c, d, e) Ag-excessive conditions. Linear fittings are applied to estimate the carrier mobility and trap density according to the space charge-limited current (SCLC) model. The regions are marked for Ohmic (Blue, $J \propto V^{n=1}$), TFL (trap-filled limited) (Green, $J \propto V^{n>2}$) and Trap-free SCLC regime (Orange, $J \propto V^{n=2}$).

Table 1
Formation energies of Ag and Bi vacancy defects from first-principles calculations.

Compound	Ag vacancy	Bi vacancy
E_{vf} (eV)	3.13	6.15

$$V_{TFL} = \frac{eN_t L^2}{2\epsilon\epsilon_0} \quad (4)$$

where e , ϵ , μ , L , V are the charge of free carriers (*i.e.*, holes), dielectric constant, carrier mobility, sample thickness, and the applied voltage bias, respectively. N_t is the density of deep traps. It is therefore possible for us to estimate the carrier mobility (μ) and trap density (N_t) by fitting the measured J_{SCL} - V curves with these formulas shown above.

The high crystallinity of our $\text{Cs}_2\text{AgBiBr}_6$ single crystals allowed us to achieve higher carrier mobility and lower trap density based on their J - V characteristics. To estimate the carrier mobility and trap density, we first measured the dielectric constants (ϵ) of the as-grown $\text{Cs}_2\text{AgBiBr}_6$ single crystals electrically (detailed information related to the dielectric permittivity measurements are in the method section and Fig. S11, Supporting Information). Then, the μ and N_t values of the as-grown $\text{Cs}_2\text{AgBiBr}_6$ single crystals were obtained *via* linear fits of the $\log J$ - $\log V$ plots). It is evident that the as-grown $\text{Cs}_2\text{AgBiBr}_6$ single crystals (μ and $N_t = 22.3 \text{ cm}^2 \text{ V}^{-1} \text{ s}^{-1}$ and $9.57 \times 10^9 \text{ cm}^{-3}$, respectively) under Ag-excess conditions (Fig. 6e) exhibit ~ 5 times higher mobility and possess approximately three times lower trap density than those (μ and $N_t = 4.47 \text{ cm}^2 \text{ V}^{-1} \text{ s}^{-1}$ and $36.0 \times 10^9 \text{ cm}^{-3}$, respectively) under stoichiometric conditions (Fig. 6a). Note that there was no noticeable difference in the surface morphologies of the as-synthesized $\text{Cs}_2\text{AgBiBr}_6$ single crystals under stoichiometric and Ag-excessive environments (Fig. S12, Supporting Information), which indicates that a difference in the measured electrical properties was not attributed to extrinsic effects such as grain boundaries. More interestingly, the obtained N_t decreased significantly as the initial Ag^+ molar concentration with respect to the Bi^{3+} molar concentration increased (Fig. S13a, Supporting Information). On the other hand, the estimated μ progressively increased with an increase in $\text{Ag}^+/\text{Bi}^{3+}$ molar ratio (Fig. S13b, Supporting Information). The highest μ value ($\sim 22.3 \text{ cm}^2 \text{ V}^{-1} \text{ s}^{-1}$) was measured in our $\text{Cs}_2\text{AgBiBr}_6$ single crystals synthesized under an Ag-abundant ($\text{Ag}^+:\text{Bi}^{3+} = 1.2 : 1$) environment. This value is comparable to the μ values (11.8 and $55.7 \text{ cm}^2 \text{ V}^{-1} \text{ s}^{-1}$) reported in previous studies [31,41].

To understand the microscopic origin of the synthetic-environment-dependent transport properties (*i.e.*, μ and N_t) in the as-grown $\text{Cs}_2\text{AgBiBr}_6$ single crystals, we predicted the formation energies of Ag and Bi vacancy defects through first-principles calculations, as shown in Table 1. To compute the vacancy formation energy (E_{vf}), we first added the energies of defective $\text{Cs}_2\text{AgBiBr}_6$ (E_{total}) (with either the Ag or Bi vacancy) and a single Ag or Bi atom ($E_{\text{Ag/Bi}}$). Then, the energy of defect-free $\text{Cs}_2\text{AgBiBr}_6$ (E_0) was subtracted from the sum of E_{total} and $E_{\text{Ag/Bi}}$ (For more details on our theoretical calculations, see the method section in Supporting Information). It is interesting that the formation energy of an Ag vacancy (3.13 eV) is about twice as low as that of a Bi vacancy (6.15 eV). Thus, the formation of these Ag vacancy defects during crystal growth can be much easier under Ag-deficient and stoichiometric environments rather than Ag-excess conditions. At a given Ag vacancy site, the primary $\text{Cs}_2\text{AgBiBr}_6$ phase would be structurally unstable resulting in the emergence of a secondary $\text{Cs}_3\text{Bi}_2\text{Br}_9$ phase (a possible scenario of a structural transition from a double perovskite $\text{Cs}_2\text{AgBiBr}_6$ phase to a layered perovskite

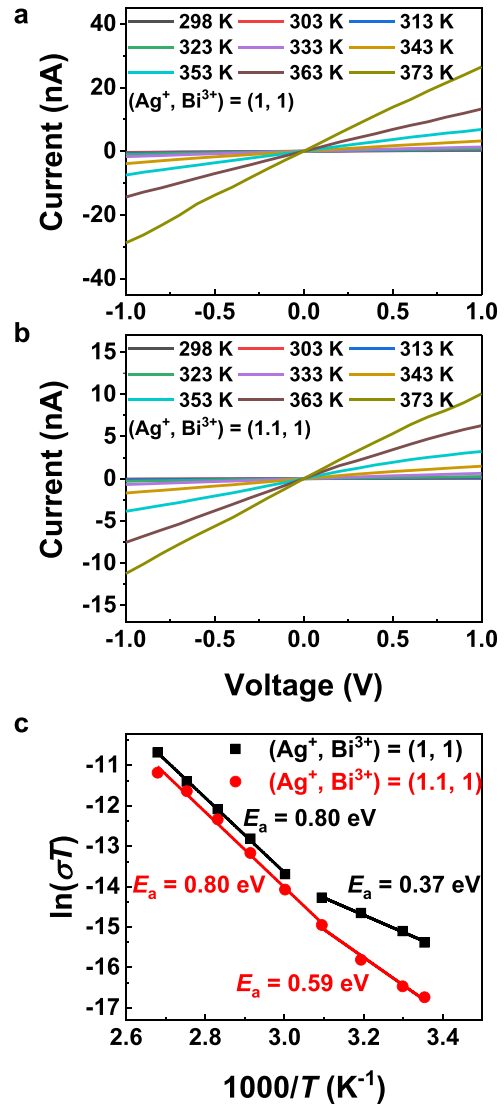


Fig. 7. (a), (b) Temperature-dependent dark current of $\text{Cs}_2\text{AgBiBr}_6$ crystal grown under various chemical environments (*i.e.*, stoichiometric (a) and Ag-excess conditions (b)). (c) Arrhenius plots of the temperature dependence of σT versus $1000/T$.

$\text{Cs}_3\text{Bi}_2\text{Br}_9$ phase is schematically described in Fig. S14, Supporting Information). The UV–visible absorption measurements of our $\text{Cs}_2\text{AgBiBr}_6$ single crystals revealed that the as-grown single crystals (2.10–2.12 eV) under Ag-excess conditions exhibited a higher indirect band gap ($E_{g,\text{indirect}}$) than those (2.07 eV) under stoichiometric conditions (Fig. S15 and Table S2, Supporting Information). Note that $E_{g,\text{indirect}}$ in $\text{Cs}_2\text{AgBiBr}_6$ was calculated to be ~ 2.26 eV in our theoretical results (Fig. S9, Supporting Information). Considering the fact that an optical band gap in a solid is usually reduced with the formation of defect levels [35,41], the as-grown $\text{Cs}_2\text{AgBiBr}_6$ single crystals under Ag-rich conditions should contain fewer Ag vacancies than those under stoichiometric conditions. Since vacancy defects in solids also act as trapping sites, impeding the movements in free charge carriers [35,41], it is highly likely that the major hole carriers are more mobile in $\text{Cs}_2\text{AgBiBr}_6$ single crystals synthesized under an Ag excess environment due to the lower concentration of charge trapping sites, which is consistent with our transport results of μ and N_t .

To get further insight on the underlying mechanism of the

enhanced transport properties in the as-grown $\text{Cs}_2\text{AgBiBr}_6$ single crystals under Ag-excessive conditions, we performed the temperature (T)-dependent conductivity measurements on $\text{Cs}_2\text{AgBiBr}_6$ single crystals, as shown in Fig. 7. We first measured the current (I)-voltage (V) characteristics of two as-grown $\text{Cs}_2\text{AgBiBr}_6$ single crystals [i.e., synthesized under stoichiometric (Fig. 7a) and Ag-excessive (Fig. 7b) conditions, respectively] in the temperature range from 298 to 373 K. Then, we plotted the measured electrical conductivity (σ) in accordance with the Arrhenius relation [$\ln(\sigma T)$ vs. $1/T$] and extracted the activation energy (E_a) for electrical transport via the subsequent linear fit of the Arrhenius plot (Fig. 7c) [31,42]. For the $\text{Cs}_2\text{AgBiBr}_6$ single crystal under a stoichiometric (Ag-excessive) condition, E_a for charge transport was estimated to 0.80 (0.80) eV at high temperatures, whereas it was 0.37 (0.59) eV at low temperatures. Note that the high-temperature transport behaviors are dominated by thermal activation of major charge carriers (i.e., mobile holes for $\text{Cs}_2\text{AgBiBr}_6$) and hence, the energy barrier height should be comparable to a half of an electronic band gap (i.e., $E_{g,\text{indirect}} \sim 2.10$ eV in our UV–visible absorption measurements of $\text{Cs}_2\text{AgBiBr}_6$ single crystals) in intrinsic semiconductors with slight variations [42]. On the contrary, E_a at low temperatures can be easily affected by extrinsic effects such as vacancy defects and interfacial Schottky barrier [31,43]. Considering that the $\text{Cs}_2\text{AgBiBr}_6$ single crystal grown under a stoichiometric condition is more defective than the as-grown single crystal under an Ag-excessive condition, the charge transport at low temperatures would be governed by extrinsic defects with a lower E_a than intrinsic charge carriers. Further studies are highly desirable to elucidate the mechanism of the defect-mediated electrical charge transport on an atomic scale.

3. Conclusions

In summary, we experimentally achieved highly crystalline lead-free double perovskite halide $\text{Cs}_2\text{AgBiBr}_6$ single crystals with a well-defined atomic ordering using a hydrothermal method. The successful growth of $\text{Cs}_2\text{AgBiBr}_6$ single crystals was achieved by systematically controlling the initial chemical environment in the hydrothermal synthesis. At the beginning stage of the hydrothermal reaction, Ag-rich conditions were used to suppress the formation of Ag vacancies in the single-crystal growth of $\text{Cs}_2\text{AgBiBr}_6$. Our results are of practical interest for fabricating high-quality lead-free halide materials and for optimizing their synthetic conditions where the reproducible growth of the halide materials is feasible. Conceptually, this work can be utilized to realize defect-free optoelectronic devices with high performance and multifunctionality.

Declaration of competing interest

The authors declare that they have no known competing financial interests or personal relationships that could have appeared to influence the work reported in this paper.

Acknowledgments

T.H.K. acknowledges the National Research Foundation of Korea (NRF) grants funded by the Ministry of Science and ICT (NRF-2020R1F1A1057220) and the Ministry of Education (NRF-2019R1A6A1A11053838). C.W.A. acknowledges the support by Basic Science Research Program through the NRF funded the Ministry of Science and ICT (NRF-2018R1A2B6009210). Y.H.H. acknowledges the support by the NRF of Korea (NRF-2019R111A3A01063856). H.Y.J. acknowledges the support from Creative Materials Discovery Program (NRF-2016M3D1A1900035). Y.-H.S. acknowledges the

support by Basic Science Research Program through the NRF funded the Ministry of Science and ICT (NRF-2018R1A2B6005159). Experiments at PLS-II were supported in part by MSICT and POSTECH.

Appendix A. Supplementary data

Supplementary data to this article can be found online at <https://doi.org/10.1016/j.jmat.2020.05.008>.

References

- [1] Lee MM, Teuscher J, Miyasaka T, Murakami TN, Snaith HJ. Efficient hybrid solar cells based on meso-superstructured organometal halide perovskites. *Science* 2012;338:643–7.
- [2] Noh JH, Im SH, Heo JH, Mandal TN, Seok SI. Chemical management for colorful, efficient, and stable inorganic–organic hybrid nanostructured solar cells. *Nano Lett* 2013;13:1764–9.
- [3] Kojima A, Teshima K, Shirai Y, Miyasaka T. Organometal halide perovskites as visible-light sensitizers for photovoltaic cells. *J Am Chem Soc* 2009;131:6050–1.
- [4] Yakunin S, Sytnyk M, Kriegner D, Shrestha S, Richter M, Matt GJ, et al. Detection of x-ray photons by solution-processed lead halide perovskites. *Nat Photonics* 2015;9:444–9.
- [5] Wei H, Fang Y, Mulligan P, Chuirazzi W, Fang H-H, Wang C, et al. Sensitive x-ray detectors made of methylammonium lead tribromide perovskite single crystals. *Nat Photonics* 2016;10:333–9.
- [6] Stoumpos CC, Malliakas CD, Peters JA, Liu Z, Sebastian M, Im J, Chasapis TC, Wibowo AC, Chung DY, Freeman AJ. Crystal growth of the perovskite semiconductor CsPbBr_3 : a new material for high-energy radiation detection. *Cryst Growth Des* 2013;13:2722–7.
- [7] Tan Z-K, Moghaddam RS, Lai ML, Docampo P, Higler R, Deschler F, Price M, Sadhanala A, Pazos LM, Credgington D. Bright light-emitting diodes based on organometal halide perovskite. *Nat Nanotechnol* 2014;9:687–92.
- [8] Cho H, Jeong S-H, Park M-H, Kim Y-H, Wolf C, Lee C-L, Heo JH, Sadhanala A, Myoung N, Yoo S. Overcoming the electroluminescence efficiency limitations of perovskite light-emitting diodes. *Science* 2015;350:1222–5.
- [9] Song J, Li J, Li X, Xu L, Dong Y, Zeng H. Quantum dot light-emitting diodes based on inorganic perovskite cesium lead halides (CsPbX_3). *Adv Mater* 2015;27:7162–7.
- [10] Min H, Kim M, Lee S-U, Kim H, Kim G, Choi K, Lee JH, Seok SI. Efficient, stable solar cells by using inherent bandgap of α -phase formamidinium lead iodide. *Science* 2019;366:749–53.
- [11] Babayigit A, Ethirajan A, Muller M, Conings B. Toxicity of organometal halide perovskite solar cells. *Nat Mater* 2016;15:247–51.
- [12] Saparov B, Hong F, Sun J-P, Duan H-S, Meng W, Cameron S, Hill IG, Yan Y, Mitzi DB. Thin-film preparation and characterization of $\text{Cs}_3\text{Sb}_2\text{I}_9$: a lead-free layered perovskite semiconductor. *Chem Mater* 2015;27:5622–32.
- [13] Fujihara T, Terakawa S, Matsushima T, Qin C, Yahiro M, Adachi C. Fabrication of high coverage MASnI_3 perovskite films for stable, planar heterojunction solar cells. *J Mater Chem C* 2017;5:1121–7.
- [14] Lyu M, Yun J-H, Cai M, Jiao Y, Bernhardt PV, Zhang M, Wang Q, Du A, Wang H, Liu G. Organic–inorganic bismuth (III)-based material: a lead-free, air-stable and solution-processable light-absorber beyond organolead perovskites. *Nano Res* 2016;9:692–702.
- [15] Damjanovic D, Klein N, Li J, Porokhonskyy V. What can be expected from lead-free piezoelectric materials? *Funct Mater Lett* 2010;3:5–13.
- [16] Nedelcu G, Protesescu L, Yakunin S, Bodnarchuk MI, Grotevent MJ, Kovalenko MV. Fast anion-exchange in highly luminescent nanocrystals of cesium lead halide perovskites (CsPbX_3 , X = Cl, Br, I). *Nano Lett* 2015;15:5635–40.
- [17] Protesescu L, Yakunin S, Bodnarchuk MI, Krieg F, Caputo R, Hendon CH, Yang RX, Walsh A, Kovalenko MV. Nanocrystals of cesium lead halide perovskites (CsPbX_3 , X = Cl, Br, and I): novel optoelectronic materials showing bright emission with wide color gamut. *Nano Lett* 2015;15:3692–6.
- [18] Slavney AH, Hu T, Lindenberger AM, Karunadasa HI. A bismuth-halide double perovskite with long carrier recombination lifetime for photovoltaic applications. *J Am Chem Soc* 2016;138:2138–41.
- [19] McClure ET, Ball MR, Windl W, Woodward PM. $\text{Cs}_2\text{AgBiX}_6$ (X = Br, Cl): new visible light absorbing, lead-free halide perovskite semiconductors. *Chem Mater* 2016;28:1348–54.
- [20] Luo J, Wang X, Li S, Liu J, Guo Y, Niu G, Yao L, Fu Y, Gao L, Dong Q. Efficient and stable emission of warm-white light from lead-free halide double perovskites. *Nature* 2018;563:541–5.
- [21] Steele JA, Pan W, Martin C, Keshavarz M, Debroye E, Yuan H, Banerjee S, Fron E, Jonckheere D, Kim CW. Photophysical pathways in highly sensitive $\text{Cs}_2\text{AgBiBr}_6$ double-perovskite single-crystal x-ray detectors. *Adv Mater* 2018;30:1804450.
- [22] Xiao Z, Meng W, Wang J, Yan Y. Thermodynamic stability and defect chemistry of bismuth-based lead-free double perovskites. *ChemSusChem* 2016;9:2628–33.
- [23] Hull S, Berastegui P. Crystal structures and ionic conductivities of ternary

derivatives of the silver and copper monohalides-II: ordered phases within the $(AgX)_x(MX)_{1-x}$ and $(CuX)_x(MX)_{1-x}$ ($M = K, Rb$ and Cs ; $X = Cl, Br$ and I) systems. *J Solid State Chem* 2004;177:3156–73.

- [24] Lazarini F. Caesium enneabromodibismuthate (III). *Acta Crystallogr B* 1977;33:2961–4.
- [25] Tubandt C. Über Elektrizitätsleitung in festen kristallisierten Verbindungen. Zweite Mitteilung. Überführung und Wanderung der Ionen in einheitlichen festen Elektrolyten. *Z Anorg Allg Chem* 1921;115:105–26.
- [26] Tuller H. Ionic conduction and applications. In: Kasap S, Capper P, editors. *Springer handbook of electronic and photonic materials*. Cham: Springer; 2017. p. 247–63.
- [27] Malugani J, Wasniewski A, Doreau M, Robert G, Al Rikabi A. Conductivite ionique dans les verres $AgPO_3-AgX$ ($X = I, Br, Cl$). *Mater Res Bull* 1978;13: 427–33.
- [28] Zurbuchen M, Lettieri J, Fulk S, Jia Y, Carim A, Schlom D, Streiffer S. Bismuth volatility effects on the perfection of $SrBi_2Nb_2O_9$ and $SrBi_2Ta_2O_9$ films. *Appl Phys Lett* 2003;82:4711–3.
- [29] Kim S, Choi E, Bhalla A. Effects of excess bismuth content in precursor solutions on ferroelectric properties of $BiFeO_3$ thin films prepared by a chemical solution deposition. *Ferroelectrics Lett Sec* 2007;34:84–94.
- [30] Watanabe H, Mihara T, Yoshimori H, de Araujo CAP. Preparation of ferroelectric thin films of bismuth layer structured compounds. *Jap J Appl Phys* 1995;34:5240–4.
- [31] Pan W, Wu H, Luo J, Deng Z, Ge C, Chen C, et al. $Cs_2AgBiBr_6$ single-crystal x-ray detectors with a low detection limit. *Nat Photonics* 2017;11:726.
- [32] Zhang M, Zheng Z, Fu Q, Chen Z, He J, Zhang S, Yan L, Hu Y, Luo W. Growth and characterization of all-inorganic lead halide perovskite semiconductor $CsPbBr_3$ single crystals. *CrystEngComm* 2017;19:6797–803.
- [33] Furukawa Y, Sato M, Kitamura K, Yajima Y, Minakata M. Optical damage resistance and crystal quality of $LiNbO_3$ single crystals with various $[Li]/[Nb]$ ratios. *J Appl Phys* 1992;72:3250–4.
- [34] Yamashita S, Kikkawa J, Yanagisawa K, Nagai T, Ishizuka K, Kimoto K. Atomic number dependence of Z contrast in scanning transmission electron microscopy. *Sci Rep* 2018;8:12325.
- [35] Yang J, Zhang P, Wei S-H. Band structure engineering of $Cs_2AgBiBr_6$ perovskite through order–disordered transition: a first-principle study. *J Phys Chem Lett* 2017;9:31–5.
- [36] Dong Q, Fang Y, Shao Y, Mulligan P, Qiu J, Cao L, Huang J. Electron-hole diffusion lengths > 175 μm in solution-grown $CH_3NH_3PbI_3$ single crystals. *Science* 2015;347:967–70.
- [37] Chiu F-C. A review on conduction mechanisms in dielectric films. *Adv Mater Sci Eng* 2014;2014:578168.
- [38] Jain A, Kumar P, Jain S, Kumar V, Kaur R, Mehra R. Trap filled limit voltage (V_{TFL}) and V^2 law in space charge limited currents. *J Appl Phys* 2007;102: 094505.
- [39] Lampert MA. Simplified theory of space-charge-limited currents in an insulator with traps. *Phys Rev* 1956;103:1648–56.
- [40] Mott NF, Gurney RW. Electronic processes in ionic crystals. *J Chem Educ* 1940;18:249.
- [41] Yuan W, Niu G, Xian Y, Wu H, Wang H, Yin H, Liu P, Li W, Fan J. In situ regulating the order–disorder phase transition in $Cs_2AgBiBr_6$ single crystal toward the application in an x-ray detector. *Adv Funct Mater* 2019;29: 1900234.
- [42] Sze SM, Ng KK. *Physics of semiconductor devices*. New Jersey: John Wiley & Sons; 2007.
- [43] Lee JW, Kim SG, Yang JM, Yang Y, Park NG. Verification and mitigation of ion migration in perovskite solar cells. *APL Mater* 2019;7:041111.



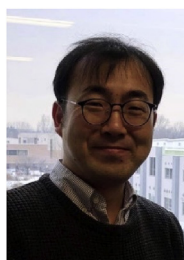
Jae Hun Jo received the B.S. degree in Physics from University of Ulsan, Republic of Korea in 2019. He is currently a M.S. candidate in Department of Physics and Energy Harvest-Storage Research Center (EHSRC), University of Ulsan, Republic of Korea. His research interests are the growth and fundamental analysis of lead-free halide perovskite single crystals.



Younghun Hwang is currently a Lector Professor in School of Electrical and Electronics Engineering / Semiconductor Applications, Ulsan College, Ulsan, Republic of Korea. He received his Ph.D. from University of Ulsan in Department of Physics in 2005. His recent research interest is focused on the synthesis of single crystals of lead-free halide perovskites, II-VI/IV-VI semiconductors, and two-dimensional materials for the applications of energy-conversion devices, radiation detector and thermoelectric. In particular, the study of optical, magneto-optical and transport characteristics of single crystals is carried out.



Sanghan Lee is currently an associate professor at Gwangju Institute of Science and Technology (GIST). He received his B.S. and M.S. degree in Materials Science and Engineering from POSTECH, Pohang, Korea in 2004 and 2006, respectively. Then, he received his Ph.D. degree in Materials Science and Engineering from University of Wisconsin-Madison in 2012 and had worked as a postdoctoral scholar in the same institution before moving to GIST in 2013. His research is highly focused on growth and characterization of various functional thin films including complex oxides and TMDs for application in energy conversion or electronic devices.



Hyoungjeen Jeon is an associate professor of physics at Pusan National University. His research interest is on chemistry–structure–property relationship in complex oxides and intermetallics. Before joining Pusan National University, he was a postdoctoral research associate in Oak Ridge National Laboratory from 2011 to 2014. He completed his Ph.D. and M.Sc. in Physics from University of Florida at 2007 and 2011. He earned his B.S. in Physics from Pusan National University at 2003.



Chang Won Ahn is currently a Research Professor in Department of Physics and Energy Harvest-Storage Research Center (EHSRC), University of Ulsan, Republic of Korea. He received his Ph.D. from University of Ulsan in Department of Physics in 2007. His recent research interest is focused on the synthesis of nanotubes, thin films and textured ceramics of lead-free piezoelectric materials for the applications of energy-conversion devices. Particular interests are photovoltaic and photocatalysis effects of nanoporous ferroelectric materials.



Young-Han Shin is a professor of physics at University of Ulsan. He received his Ph.D from Korea Advanced Institute of Science and Technology in 2001, and held postdoctoral positions at Sejong University, University of Pennsylvania. He came to POSTECH as a research professor in 2006. Dr. Shin's research areas include computational chemistry, physics, and materials.



Hu Young Jeong received the B.S. degree in Materials Science and Engineering from Pohang University of Science and Technology (POSTECH), Pohang, Korea in 2003 and the Ph.D. degree from the Department of Materials Science and Engineering of Korea Advanced Institute of Science and Technology (KAIST) in 2010. He is currently an Associate Professor in UNIST Central Research Facilities, Ulsan National Institute of Science and Technology (UNIST) since 2016. His research interests include the nano-material characterization using advanced transmission electron microscope (TEM).



Ill Won Kim is currently an advisory professor of physics at the University of Ulsan, Republic of Korea. He obtained MS degrees in Physics in 1982 and PhD degree in ferroelectric science in 1988, from Busan National University, South Korea. On graduation, he joined the University of Ulsan as a faculty member. He has held visiting appointments at the Materials Research Laboratory in

Pennsylvania State University, USA and JAIST in Japan, and also study RCDAMP at Pusan National University, Republic of Korea. His main research includes the investigation of lead-free ferroelectric and piezoelectric thin films, the development of texture in lead-free bulk ceramic piezoelectrics, and ferroelectric energy harvesting materials.



Tae Heon Kim is currently an assistant professor in Department of Physics, University of Ulsan (UoU), Ulsan, Republic of Korea since 2016. He received the B.S. degree in Physics from Seoul National University, Seoul, Korea in 2006 and the Ph.D. degree in Physics from Seoul National University, Seoul, Korea in 2012. Before joining UoU as the faculty member, he had worked in University of Wisconsin-Madison, Madison, USA as a Postdoctoral Researcher. His research interests are to design novel multi-functional materials and to explore exotic phenomena in their physical properties.